Journal of Computational and Applied Mathematics 234 (2010) 2089–2097

Contents lists available at ScienceDirect

Journal of Computational and Applied Mathematics

journal homepage: www.elsevier.com/locate/cam

# Resolution of computational aeroacoustics problems on unstructured grids with a higher-order finite volume scheme☆

X. Nogueira [a,*], I. Colominas [a], L. Cueto-Felgueroso [b], S. Khelladi [c], F. Navarrina [a], M. Casteleiro [a]

[a] Group of Numerical Methods in Engineering, Universidade da Coruña, Civil Eng. School, Campus de Elviña, 15071, A Coruña, Spain

[b] Department of Civil and Environmental Engineering, MIT, 77 Massachusetts Ave 48-108, Cambridge, MA 02139, USA

[c] Arts et Métiers ParisTech, 151 boulevard de l'Hôpital, 75013 Paris, France

ARTICLE INFO

*Article history:*
Received 3 September 2008
Received in revised form 27 February 2009

*Keywords:*
Computational aeroacoustics
Finite volume method
Moving Least Squares
Unstructured grids

ABSTRACT

Computational fluid dynamics (CFD) has become increasingly used in the industry for the simulation of flows. Nevertheless, the complex configurations of real engineering problems make the application of very accurate methods that only work on structured grids difficult. From this point of view, the development of higher-order methods for unstructured grids is desirable. The finite volume method can be used with unstructured grids, but unfortunately it is difficult to achieve an order of accuracy higher than two, and the common approach is a simple extension of the one-dimensional case. The increase of the order of accuracy in finite volume methods on general unstructured grids has been limited due to the difficulty in the evaluation of field derivatives. This problem is overcome with the application of the Moving Least Squares (MLS) technique on a finite volume framework. In this work we present the application of this method (FV-MLS) to the solution of aeroacoustic problems.



## 1. Introduction

The simulation of sound propagation in the air is a very difficult numerical problem [1]. If we try to solve an acoustic problem with the same methods as developed for aerodynamics, a lot of numerical difficulties arise that are not present in the resolution of aerodynamic problems. The origin of such difficulties relies on the nature of the acoustic problem. The low magnitude of acoustic waves makes the use of low dissipation schemes mandatory, and it complicates even more the problem of the boundary conditions. Thus, the acceptable amplitude of reflections caused by waves leaving the domain is much smaller than in typical aerodynamic problems. Another feature of aeroacoustic problems is that the range of frequencies of interest is wider than in aerodynamics.

In computational aeroacoustics (CAA), the most successful numerical schemes have been spectral methods or high-resolution finite differences [2,3]. These methods work very well on structured grids, but unfortunately they present problems when applied to the resolution of problems with complex geometries. In this context, the development of methods that can solve CAA problems on unstructured grids is interesting. The finite volume method, widely and successfully used for the simulation of aerodynamics with unstructured grids, presents difficulties when it is applied to aeroacoustic problems in its most usual formulation (at most order two), due to the lack of resolution of the scheme. Even though raising the order

☆ This work has been partially supported by the *Ministerio de Educación y Ciencia* of the Spanish Government (#DPI2006-15275 and #DPI2007-61214) cofinanced with FEDER funds, by the *Autonomous Government* of the *Xunta de Galicia* (Grant #PGDIT06TAM11801PR and file #2007/09) and by the *Universidade da Coruña*.

* Corresponding author.
*E-mail addresses:* xnogueira@udc.es (X. Nogueira), icolominas@udc.es (I. Colominas).
*URL:* http://caminos.udc.es/gmni (I. Colominas).

0377-0427/$ – see front matter © 2009 Elsevier B.V. All rights reserved.
doi:10.1016/j.cam.2009.08.067

is not the only (nor probably the best) way to improve the resolution of the schemes, it is the most usual approach on unstructured grids, due to the difficulty in generalizing the methods developed for structured meshes [4]. But this approach is also not obvious, and the main problem is the evaluation of high-order derivatives. The FV-MLS method [5–7] overcomes this difficulty by using the Moving Least Squares (MLS) technique [8] to compute the gradients and successive derivatives. Thus, it builds higher-order schemes in a finite volume framework without the introduction of new degrees of freedom.

The aim of this work is to extend the application of the FV-MLS method to the resolution of aeroacoustic problems, by focusing our attention on the resolution of the Linearized Euler Equations (LEEs). Moreover, the multiresolution features of the MLS approach [9] allow the development of low-pass filters that could be used together with a grid-stretching technique to build an absorbing layer that avoids reflections at the boundaries, following the methodology exposed in [10].

## 2. Linearized Euler equations

Most aeroacoustic problems are linear, so it is possible to linearize the Euler equations around a (mean) stationary solution $\boldsymbol{U_0} = (\rho_0, u_0, v_0, p_0)$. Then, the 2D LEEs written in conservative form are the following:

$$\frac{\partial \boldsymbol{U}}{\partial t} + \frac{\partial \boldsymbol{E}}{\partial x} + \frac{\partial \boldsymbol{F}}{\partial y} + \boldsymbol{H} = \boldsymbol{S} \tag{1}$$

where $\boldsymbol{S}$ is a source term and

$$\boldsymbol{U} = \begin{pmatrix} \rho' \\ u' \\ v' \\ p' \end{pmatrix} \qquad \boldsymbol{E} = \begin{pmatrix} \rho' u_0 + \rho_0 u' \\ \dfrac{p'}{\rho_0} + u_0 u' \\ u_0 v' \\ u_0 p' + \gamma p_0 u' \end{pmatrix} \qquad \boldsymbol{F} = \begin{pmatrix} \rho' v_0 + \rho_0 v' \\ v_0 u' \\ \dfrac{p'}{\rho_0} + v_0 v' \\ v_0 p' + \gamma p_0 v' \end{pmatrix} \tag{2}$$

$$\boldsymbol{H} = \begin{pmatrix} 0 \\ \dfrac{\left(\rho_0 u' + u_0 \rho'\right)}{\rho_0} \dfrac{\partial u_0}{\partial x} + \dfrac{\left(\rho_0 v' + v_0 \rho'\right)}{\rho_0} \dfrac{\partial u_0}{\partial y} \\ \dfrac{\left(\rho_0 u' + u_0 \rho'\right)}{\rho_0} \dfrac{\partial v_0}{\partial x} + \dfrac{\left(\rho_0 v' + v_0 \rho'\right)}{\rho_0} \dfrac{\partial v_0}{\partial y} \\ (\gamma - 1)\, p' \nabla \cdot \boldsymbol{v}_0 - (\gamma - 1)\, u' \nabla p_0 \end{pmatrix} \tag{3}$$

where the velocity is $\boldsymbol{v} = (u, v)$, $\rho$ is the density, $p$ the pressure, and $\gamma = 1.4$. The subscript $_0$ refers to mean values and $'$ indicates perturbation quantities around the mean. In case of a uniform mean flow, $\boldsymbol{H}$ is null.

## 3. Numerical method

### 3.1. An MLS-based finite volume scheme

A method based on the application of Moving Least Squares (MLS) to compute the derivatives in a finite volume framework (FV-MLS) [5,6] has been used to discretize the LEEs (1). Fluxes are discretized with a flux vector splitting method. In order to increase the order achieved by the method, a Taylor expansion of the variable is performed at the interior of each cell. Next, the approximation of the higher-order derivatives needed to compute the Taylor reconstruction is obtained by an MLS approach. Thus, if we consider a function $\Phi(\boldsymbol{x})$ defined in a domain $\Omega$, the basic idea of the MLS approach is to approximate $\Phi(\boldsymbol{x})$, at a given point $\boldsymbol{x}$, through a weighted least-squares fitting of $\Phi(\boldsymbol{x})$ in a neighborhood of $\boldsymbol{x}$ as

$$\Phi(\boldsymbol{x}) \approx \widehat{\Phi}(\boldsymbol{x}) = \sum_{i=1}^{m} p_i(\boldsymbol{x})\, \boldsymbol{\alpha}_i(\boldsymbol{z})\,|_{\boldsymbol{z}=\boldsymbol{x}} = \boldsymbol{p}^{\mathrm{T}}(\boldsymbol{x})\, \boldsymbol{\alpha}(\boldsymbol{z})\,|_{\boldsymbol{z}=\boldsymbol{x}}. \tag{4}$$

$\boldsymbol{p}^{\mathrm{T}}(\boldsymbol{x})$ is an $m$-dimensional polynomial basis and $\boldsymbol{\alpha}(\boldsymbol{z})|_{\boldsymbol{z}=\boldsymbol{x}}$ is a set of parameters to be determined, such that they minimize the following error functional:

$$J(\boldsymbol{\alpha}(\boldsymbol{z})|_{\boldsymbol{z}=\boldsymbol{x}}) = \int_{\boldsymbol{y}\in\Omega_{\boldsymbol{x}}} W(\boldsymbol{z}-\boldsymbol{y}, h)|_{\boldsymbol{z}=\boldsymbol{x}} \left[\Phi(\boldsymbol{y}) - \boldsymbol{p}^{\mathrm{T}}(\boldsymbol{y})\boldsymbol{\alpha}(\boldsymbol{z})|_{\boldsymbol{z}=\boldsymbol{x}}\right]^2 \mathrm{d}\Omega_{\boldsymbol{x}}, \tag{5}$$

$W(\boldsymbol{z}-\boldsymbol{y}, h)|_{\boldsymbol{z}=\boldsymbol{x}}$ being a *kernel* with compact support (denoted by $\Omega_{\boldsymbol{x}}$) centered at $\boldsymbol{z} = \boldsymbol{x}$. The parameter $h$ is the smoothing length, which is a measure of the size of the support $\Omega_{\boldsymbol{x}}$ [5].

In this work the following polynomial cubic basis is used:

$$\boldsymbol{p}(\boldsymbol{x}) = \begin{pmatrix} 1 & x & y & xy & x^2 & y^2 & x^2y & xy^2 & x^3 & y^3 \end{pmatrix}^{\mathrm{T}}, \tag{6}$$

which provides cubic completeness. In the above expression, $(x, y)$ denotes the Cartesian coordinates of $\boldsymbol{x}$. In order to improve the conditioning, the polynomial basis is locally defined and scaled: if the shape functions are evaluated at $\boldsymbol{x}_I$,

the polynomial basis is evaluated at $(\boldsymbol{x}-\boldsymbol{x}_I)/h$. From a practical point of view, for each point $I$ we need to define a set of neighbors inside the compact support $\Omega_{\boldsymbol{x}}$. Following [5], the interpolation structure can be identified as

$$\widehat{\Phi}_I(\boldsymbol{x}) = \boldsymbol{p}^{\mathrm{T}}(\boldsymbol{x})\,\boldsymbol{\alpha}(\boldsymbol{z})\,|_{\boldsymbol{z}=\boldsymbol{x}} = \boldsymbol{p}^{\mathrm{T}}(\boldsymbol{x})\boldsymbol{M}^{-1}(\boldsymbol{x})\boldsymbol{P}_{\Omega_{\boldsymbol{x}}}\boldsymbol{W}(\boldsymbol{x})\boldsymbol{\Phi}_{\Omega_{\boldsymbol{x}}} = \boldsymbol{N}^{\mathrm{T}}(\boldsymbol{x})\boldsymbol{\Phi}_{\Omega_{\boldsymbol{x}}} = \sum_{j=1}^{n_{\boldsymbol{x}_I}} N_j(\boldsymbol{x})\Phi_j. \tag{7}$$

In the above, $n_{\boldsymbol{x}_I}$ is the number of neighbors of the cell $I$. Moreover, $\boldsymbol{M} = \boldsymbol{P}_{\Omega_{\boldsymbol{x}}}\boldsymbol{W}(\boldsymbol{x})\boldsymbol{P}^{\mathrm{T}}_{\Omega_{\boldsymbol{x}}}$ is the moment matrix. We also define the matrices $\boldsymbol{P}_{\Omega_{\boldsymbol{x}}} = (\boldsymbol{p}(x)_1 \cdots \boldsymbol{p}(x)_{n_{\boldsymbol{x}_I}})$, $\boldsymbol{\Phi}_{\Omega_{\boldsymbol{x}}} = (\Phi(x_1)\cdots\Phi(x_{n_{\boldsymbol{x}_I}}))$ and $\boldsymbol{W}(\boldsymbol{x}) = \mathrm{diag}(W_i(\boldsymbol{x}))$ with $i = 1,\ldots,n_{\boldsymbol{x}_I}$ (see [5]).

The approximation is written in terms of the MLS "shape functions" $\boldsymbol{N}^{\mathrm{T}}(\boldsymbol{x})$. The derivatives of $\boldsymbol{N}^{\mathrm{T}}(\boldsymbol{x})$ can be used to compute an approximation to the derivatives of the function. So, the gradient of $\widehat{\Phi}(\boldsymbol{x})$ is evaluated as

$$\nabla\widehat{\Phi}(\boldsymbol{x}) = \sum_{j=1}^{n_{\boldsymbol{x}_I}} \Phi_j \nabla N_j(\boldsymbol{x}). \tag{8}$$

The equation to be solved results from the application of the finite volume discretization to Eq. (1):

$$A_I\frac{\partial \boldsymbol{U}_I}{\partial t} = \sum_{iedge=1}^{nedge_I}\sum_{iq=1}^{nq_I}[-\boldsymbol{\mathcal{F}}\cdot\boldsymbol{n}]_{iq}\,\mathcal{W}_{iq} + \boldsymbol{S}_I, \tag{9}$$

where $\boldsymbol{\mathcal{F}} = (\boldsymbol{E}_x, \boldsymbol{F}_y)$, $A_I$ is the area of cell $I$, $nedge_I$ the number of cell edges, and $\boldsymbol{U}_I$ and $\boldsymbol{S}_I$ are the average values of $\boldsymbol{U}$ and $\boldsymbol{S}$, respectively, over the cell $I$ (associated to the cell centroid). $\mathcal{W}$ are the integration weights and $nq_I$ is the number of integration points. $\boldsymbol{\mathcal{F}}\cdot\boldsymbol{n}$ is computed with a standard flux vector splitting technique.

We compute the first and second derivatives required for the Taylor reconstruction of the variables at quadrature points at the edges by using Eq. (8), in a context of generalized Godunov's methods. In the case of unsteady problems, this reconstruction needs to use correction terms in order to ensure that the average value of the reconstructed variables over a cell $I$ is the centroid value $\boldsymbol{U}_I$ [5–7]. The resulting scheme is a third-order method.

The neighbors of each cell centroid $I$ of the grid are the centroids of the neighboring cells. For boundary cells, we add nodes (ghost nodes) placed in the middle of the edge defining the boundary. The definition of the stencil for each cell is done at the beginning of the calculations. An exponential kernel has been used, defined in one dimension as

$$W(x, x^*, \kappa_x) = \frac{\mathrm{e}^{-\left(\frac{s}{c}\right)^2} - \mathrm{e}^{-\left(\frac{d_m}{c}\right)^2}}{1 - \mathrm{e}^{-\left(\frac{d_m}{c}\right)^2}}, \tag{10}$$

with $s = |x - x^*|$, $d_m = \max(|x_i - x^*|)$, $i = 1,\ldots,n_{\boldsymbol{x}_I}$; $x^*$ is the reference point (the point around which the stencil moves, in this case the centroid of each cell, $I$), $x$ is the position of every cell centroid of the stencil and $\kappa_x$ is a shape parameter. Moreover, we define $c = \frac{d_m}{2\kappa_x}$.

A 2D kernel is obtained by multiplying two 1D kernels:

$$W_j(\boldsymbol{x}, \boldsymbol{x}^*, \kappa_x, \kappa_y) = W_j(x, x^*, \kappa_x)W_j(y, y^*, \kappa_y). \tag{11}$$

In this work we have used the values $\kappa_x = \kappa_y = 2.5$.

More details about the FV-MLS method can be found in [5–7].

### 3.2. Boundary conditions

Absorbing boundary conditions have been implemented by using an absorbing layer based on grid stretching. Grid stretching transfers the energy of the wave into increasingly higher wavenumber modes and the numerical scheme removes this high-frequency content. With this process the energy of the wave is dissipated. This becomes clear by looking at Fig. 1, where the dispersion and dissipation properties of the FV-MLS scheme are shown. These properties are related to the real and complex parts of the numerical wavenumber $\kappa^*$. For a high wavenumber $\kappa$ the numerical method introduces more dissipation.

On the other hand, it is possible to increase the dissipation in the absorbing layer by using the MLS method as a filter. The filtering process is developed by the application of an MLS reconstruction of the variables, i.e.,

$$\bar{\Phi}(\boldsymbol{x}) = \sum_{j=1}^{n_{\boldsymbol{x}_I}} \Phi(\boldsymbol{x})N_j(\boldsymbol{x}), \tag{12}$$

where $\Phi$ is a variable, $\bar{\Phi}$ is the filtered variable and $N$ is the MLS shape function. This reconstruction is performed by using a kernel with shape parameters with more dissipative behavior than the ones used to the approximation of the variables. The value of these parameters determines the range of frequencies to be filtered. In the case of applying an MLS-based filter, as

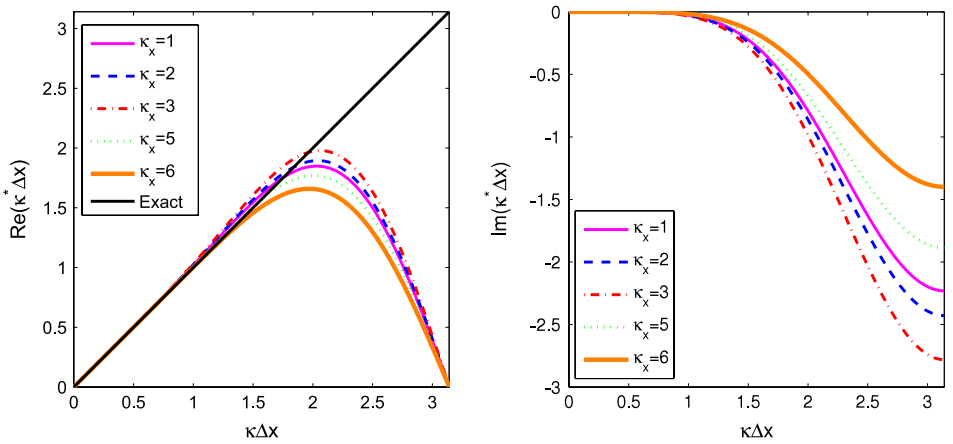


**Fig. 1.** Dispersion (left) and dissipation (right) properties of the FV-MLS method for different values of the shape parameter of the exponential kernel $\kappa_x$.

a general rule, it is suggested to filter progressively. The most aggressive filtering must be done near the outlet boundary at the end of the absorbing layer. Filtering may be progressively applied by modifying the shape parameters of the exponential kernel, in analogy to the method proposed in [11]. Dissipation properties of the FV-MLS method make the application of the explicit MLS-based filter unnecessary. Thus, in this work, explicit filtering is not applied, but it may be useful for other methods working on unstructured grids with not enough implicit dissipation.

## 4. Numerical examples

In this section we present some aeroacoustic test problems solved on unstructured grids. Most of the examples in the literature are solved on Cartesian grids by using spectral or high-resolution finite difference methods. These methods are the best in terms of spectral resolution, but present difficulties when applied to complex geometries. At this point the FV-MLS method becomes very interesting, because it allows the resolution of problems in unstructured grids with a higher-order numerical scheme. An explicit fourth-order Runge–Kutta scheme was used for the computations.

### *4.1. Source radiation in a uniform mean flow*

Here we reproduce the example of [12]. We compute the radiation of a periodic source in two cases: in a subsonic and in a supersonic mean flow. The source is located at $x_s = y_s = 0$, and it is defined as

$$S_p = \frac{1}{2}\exp\left(-\ln(2)\frac{x^2+y^2}{2}\right)\sin(\omega t)\times[1,0,0,1]^{\mathrm{T}}, \tag{13}$$

where the angular frequency is $\omega = 2\pi/30$ and $t$ is the time coordinate. The wavelength is $\lambda = 30$ units, and the computational domain is the circle with radius $r = 100$ units. The source term is made dimensionless with $[\rho_\infty c_\infty/\Delta x, 0, 0, \rho_\infty c_\infty^3/\Delta x]^{\mathrm{T}}$. In order to avoid spurious reflections at boundaries, an absorbing layer has been placed surrounding the computational domain. With the aim of testing the stability and the behavior of the proposed method for the boundary conditions, an unstructured absorbing layer has been constructed, although in general it is recommended to use a structured mesh. The absorbing layer is placed from the boundary of the computational domain to $x = \pm 300$ and $y = \pm 300$. Fig. 2 shows the grid used for the resolution of this problem. To build this grid we have placed 632 equally spaced nodes at the circumference defining the computational domain, and 20 nodes on each edge at the outer boundary.

First, we analyze the subsonic case with Mach number $M_x = 0.5$. Two acoustic waves propagate upstream and downstream of the source. Due to the effect of the mean flow, the apparent wavelength is modified. Thus, it is different upstream ($\lambda_1 = (1 - M_x)\lambda$) and downstream ($\lambda_2 = (1 + M_x)\lambda$) of the source. In Fig. 3, pressure isocontours for different non-dimensional times $t$ are shown. They are barely different from the results obtained in [12] on a Cartesian grid with the Dispersion Relation Preserving (DRP) scheme [3]. The pressure profile along the axis $y = 0$ at time $t = 270$ is reproduced in Fig. 6 (left). It is in good agreement with the analytical solution and it matches the results obtained in [12].

In order to check the stability of the boundary conditions, we let the computations to continue until $t = 5400$. This corresponds to 180 periods of the source, a time long enough for the wave to travel until the boundary and to be reflected. The results are shown in Fig. 4 (left). Comparing the pressure field with the one corresponding to $t = 270$ (9 source periods), it is observed that there is no change in the solution. The good behavior of the absorbing layer is also shown in Fig. 4 (right) at time $t = 5400$. The acoustic wave is completely dissipated when it leaves the computational domain. We note the good results despite the use of a low-quality grid for the absorbing layer. We also note that we use a third-order scheme in the

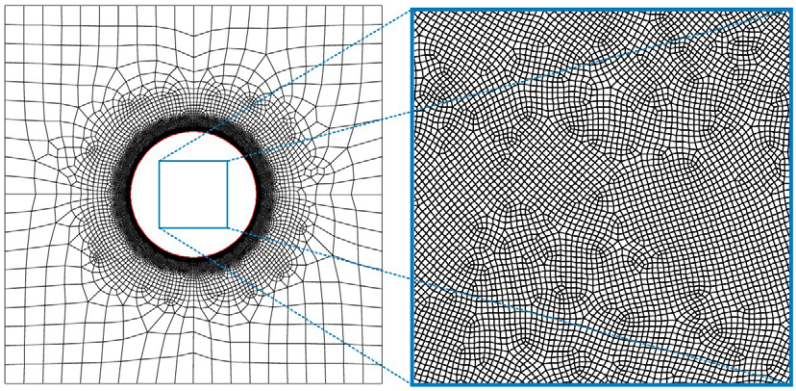

**Fig. 2.** Periodic source in a subsonic ($M = 0.5$) uniform mean flow. Absorbing layer (the grid for the computational domain is skipped for clarity) (left) and computational domain grid detail (right).

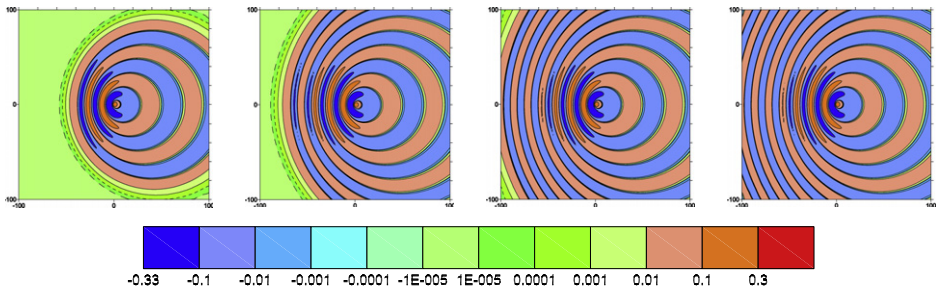


**Fig. 3.** Periodic source in a subsonic ($M = 0.5$) uniform mean flow. From left to right, pressure contours at times $t = 90$, $t = 150$, $t = 210$, and $t = 270$.

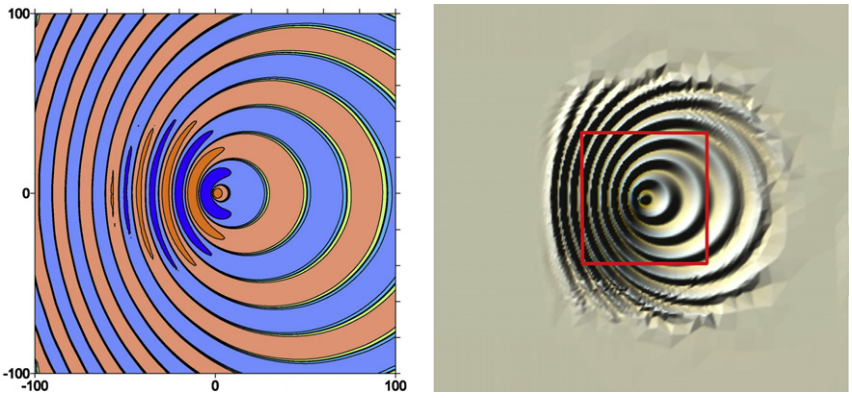


**Fig. 4.** Periodic source in a subsonic ($M = 0.5$) uniform mean flow at time $t = 5400$. Pressure contours in the computational domain are shown on the left, and the behavior of the absorbing layer is shown on the right. The acoustic waves are dissipated when they leave the computational domain indicated by the red square. The distorted waves that appear next to the front wave are located in the absorbing layer.

absorbing zone. In this zone, it is possible to use a lower-order scheme, but this would generate oscillations. In order to avoid them, we have preferred to use the same scheme in all the domains.

On the other hand, it is interesting to check if the scheme can accurately reproduce the interactions between the traveling waves. To this end, we compute the same problem in a supersonic uniform flow. In this case, the radiated field is completely different. Now, the two pressure waves propagate downstream of the source with velocity $M \pm 1$, and interference phenomena take place. The location of the source given by Eq. (13) is $(x_s, y_s) = (-50, 0)$. We use the same grid as in the previous case. The results (Figs. 5 and 6 on the right) agree quite well with the analytical solution and with those obtained in [12]. The disagreement between the analytical and the computed solution for the supersonic case in the neighborhood of the location of the source has been reported by other authors (see [12]), and it could be related to the calculation of the convolution product of the analytical solution rather than the computed solution.

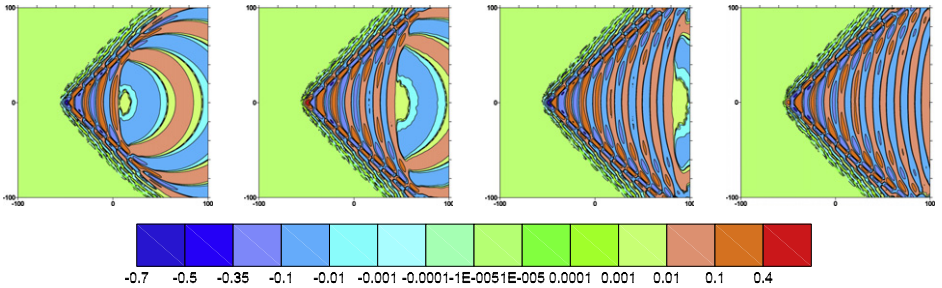


**Fig. 5.** Periodic source in a supersonic ($M = 1.5$) uniform mean flow. From left to right, pressure contours at times $t = 114$, $t = 190$, $t = 266$, and $t = 304$.

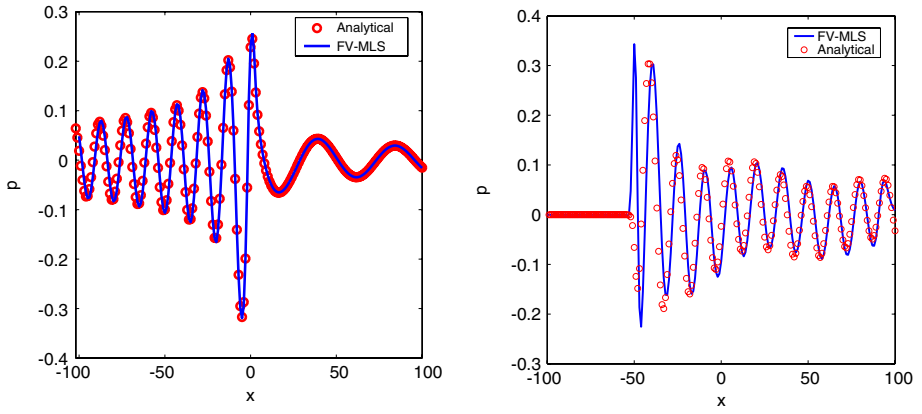


**Fig. 6.** Pressure profile along the axis $y = 0$ for a periodic source in a uniform mean flow. Left: Subsonic flow ($M = 0.5$) at $t = 270$. Right: Supersonic flow ($M = 1.5$) at $t = 304$. The circles show the analytical solution given by Bailly and Juvé [12].

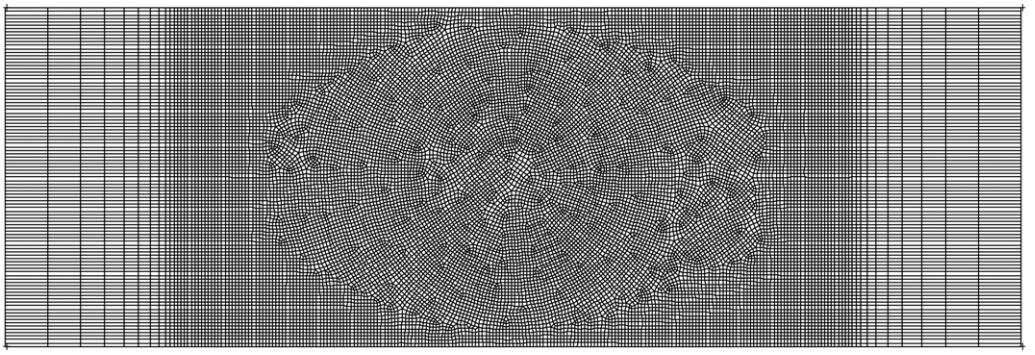

**Fig. 7.** Propagation of a wall-bounded acoustic pulse $M_x = 0.5$. Unstructured grid.

### *4.2. Propagation of a wall-bounded acoustic pulse*

This example simulates the propagation of an acoustic pulse inside a duct, in an uniform mean flow $M = 0.5$. This problem is taken from [13], where it is solved by using a fourth-order seven-point DRP scheme on a Cartesian grid, and with PML boundary conditions. This example is used to show the suitability of the method for turbomachinery applications and duct acoustics. The computational domain is defined by two solid walls placed at $y = -50$ and $y = 50$, with the $x$-coordinate varying from $-100$ to 100. An absorbing layer with length 50 units is placed at the inflow and at the outflow. Fig. 7 shows the grid used in this example. It has been built by placing a circle with radius 40 units at the centre of the duct, and meshing it with a paving scheme, with 252 points over the circumference. The total number of elements of the grid is 20,330. Each absorbing layer has 1000 elements. Only implicit filtering has been considered.

The following initial pressure disturbance is placed at $(-50,0)$:

$$p'(x, y) = \exp\left(-\ln(2)\frac{(x+50)^2 + y^2}{36}\right). \tag{14}$$

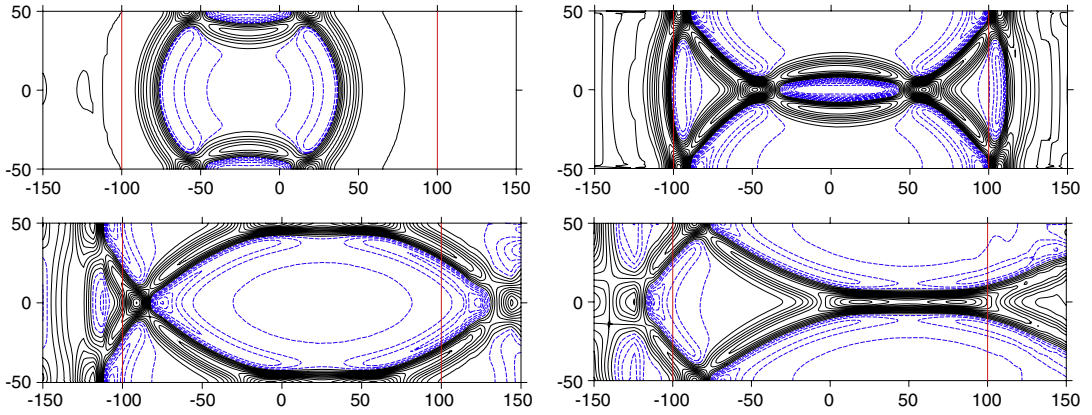


**Fig. 8.** Propagation of a wall-bounded acoustic pulse $M_x = 0.5$. Pressure fluctuation contours for $t = 60$ (top left), $t = 110$ (top right), $t = 150$ (bottom left), and $t = 200$ (bottom right). Dotted lines indicate negative values of $p'$. Vertical lines shows where the absorbing layers start.

The acoustic pulse is convected downstream, and it is reflected at the walls. In order to compare with the results presented in [10,13], we show the pressure contours at non-dimensional times $t = 60$, $t = 110$, $t = 150$, and $t = 200$ in Fig. 8. The results are comparable to those of [10,13], and no spurious reflections have been noticed.

### 4.3. Vortex convection in a uniform mean flow

The LEEs support the propagation of entropy, vorticity and acoustic waves. Entropy waves consist of density fluctuations, whereas vorticity waves consist of velocity fluctuations. Acoustic waves involve fluctuations in all the physical variables. When the vorticity and entropy waves arrive at boundaries, they can generate strong spurious acoustic waves that propagate and spoil the solution. We are going to check the ability of the method to deal with these waves. The example taken from the Acoustic Database [14] is reproduced here: the convection of a vortex in a subsonic ($M_x = 0.5$) uniform mean flow. The vortex is defined as follows:

$$p_0(\boldsymbol{x}) = \frac{1}{\gamma}, \qquad u(\boldsymbol{x}) = u_0 + u' = M_x + \epsilon y \exp\left(-\ln(2)\frac{x^2+y^2}{b^2}\right)$$
$$\rho_0(\boldsymbol{x}) = 1, \qquad v(\boldsymbol{x}) = v' = -\epsilon x \exp\left(-\ln(2)\frac{x^2+y^2}{b^2}\right) \tag{15}$$

with $b = 5$ and $\epsilon = 0.03$.

An explicit Low Dispersion and Dissipation Runge–Kutta scheme (LDDRK) [2] with four steps has been used for the calculations. We solve this problem in both a structured and an unstructured grid, to compare the effect of the second grid on the generation of spurious waves. In order to evaluate the magnitude of the reflections generated by the vortex when it leaves the computational domain, it is useful to compute the time evolution of the residual fluctuating pressure, $L_p$, defined by

$$L_p = \sqrt{\left[\frac{1}{N}\sum_{i=1}^{N}(p - p_0)^2\right]}, \tag{16}$$

where $N$ is the number of cells in the interior of the computational domain.

#### 4.3.1. Computations on a structured grid

For the Cartesian grid, the computational domain is defined as $-50 \le x \le 50$, $-50 \le y \le 50$, with $\Delta x = \Delta y = 1$. An absorbing layer is placed from $x = 50$ to $x = 200$.

The configuration parameters of the absorbing layer are critical for vorticity waves. Unfortunately, there is no universal optimal configuration of the absorbing layer, since it is problem dependent. In Fig. 9 (right) the absorbing layer built with 30 cells gives better results than the one defined with 50 cells. In finite difference methods spurious oscillations will appear if the metrics are not smooth enough. With the FV-MLS approximation, the metrics are not so critical, and the more dissipative effect of a bigger cell size predominates. However, although the metrics dependence is not so important, it is advisable to build the absorbing layer with a smooth transition from the end of the computational domain to avoid the generation of spurious acoustic waves. To this end, we place an absorbing zone divided into two parts. In the first part, a very smooth rate of growth has been applied to the 20 first cells. A more aggressive rate of growth has been applied to the last 10 cells.

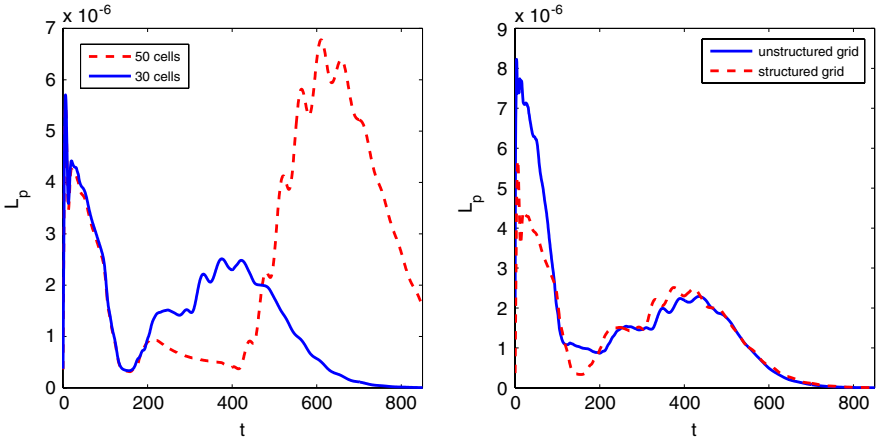


**Fig. 9.** Vortex convection in a uniform mean flow. On the left, we plot the effect of the number of cells of the absorbing layer in the residual fluctuating pressure, $L_p$. On the right, we plot the comparison of the results on the structured and on the unstructured grids.

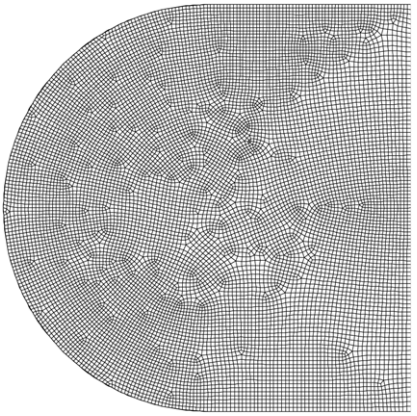

**Fig. 10.** Unstructured grid used for the vortex convection in a uniform mean flow problem. The absorbing layer is not shown.

The results are comparable to those obtained in [14] by using a DRP scheme. The bigger difference in the magnitude of $L_p$ occurs at the beginning of the calculations, and it could be related to the fact that in [14] damping terms have been used in the time integration scheme that have not been used here.

*4.3.2. Computations on an unstructured grid*

We solve the problem of the convection of a vortex on an unstructured grid. Due to the irregularity of the grid, the magnitude of the spurious oscillations produced by initial transitional acoustic waves is bigger than in the previous case. The unstructured grid used in this case is shown in Fig. 10. It has 11,476 cells in the calculation domain and the same absorbing layer as for the structured case.

The results are shown in Fig. 9 (left). As expected, the magnitude of pressure fluctuations is bigger than those obtained on a structured grid, but the results are satisfactory. In Fig. 11, we show the dissipation of the vorticity inside the absorbing layer. In Fig. 12, we plot the spurious acoustic waves entering the computational domain. The results may improve with the use of a smoother grid, made with triangular elements.

## 5. Conclusions

The application of the FV-MLS method to solve aeroacoustic problems on unstructured grids has been presented. Some numerical tests for the resolution of the Linearized Euler Equations (LEEs) with uniform mean flow have been performed. The results obtained for the propagation of acoustic waves are in good agreement with the results obtained with finite difference methods on Cartesian grids.

The dissipation of the highest frequencies performed by the FV-MLS method implicitly allows the development of an absorbing layer technique based on grid stretching. This approach has proved to be very stable and robust, and good results are obtained for the dissipation of both acoustic and vorticity waves, that could be present in many aeroacoustic problems.

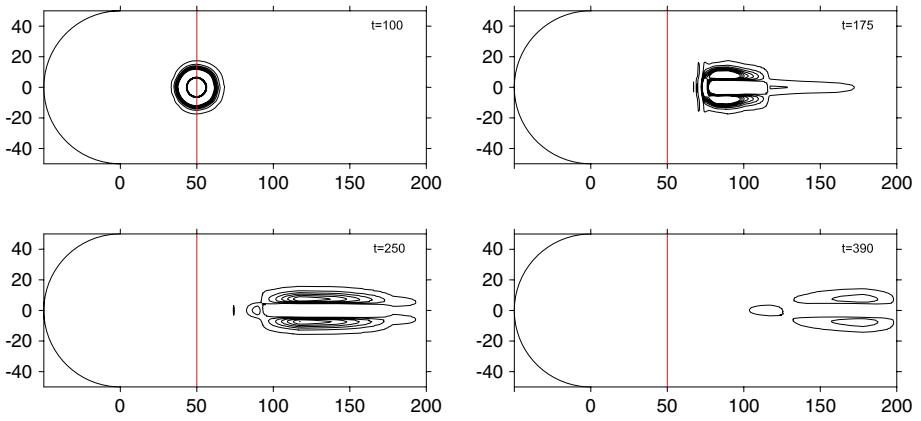


**Fig. 11.** Vorticity evolution in the absorbing layer. We plot eight vorticity contours, from $1 \times 10^{-4}$ to $36 \times 10^{-4}$ for different times. The line at $x = 50$ indicates the start of the absorbing layer.

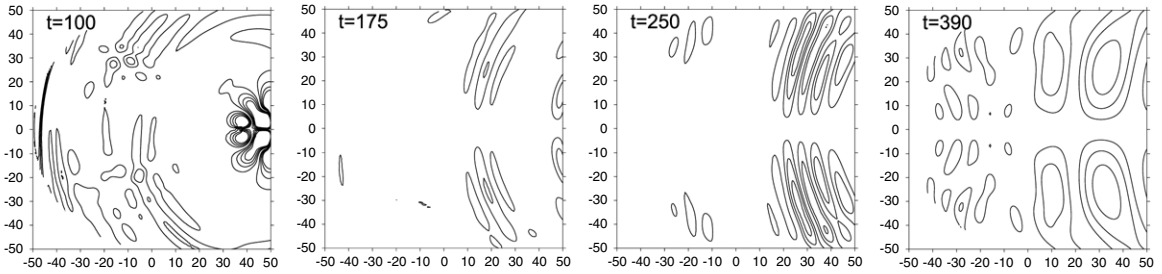


**Fig. 12.** Evolution of the spurious pressure waves in the computational domain of the unstructured grid. We plot eight pressure contours, from $-8 \times 10^{-6}$ to $8 \times 10^{-6}$ for different times. For $t = 100$, pressure waves related to numerical noise at the beginning of the computations can be still observed.

For acoustic waves, the proposed method works even with an unstructured low-quality grid. For this kind of wave, the absorbing layer presents low grid metrics dependence. Vorticity waves are more sensitive to the variation of the cell size in the absorbing layer, and the use of structured sponge zones is advisable. On the other hand, by using the FV-MLS scheme there is no need to use explicit filtering. However, an MLS-based filter may be used with other less dissipative methods on unstructured grids.

It is worth noting that although all the examples in this paper solve the LEEs, both the FV-MLS method and the MLS-based absorbing layer are able to work with nonlinear equations.

## References

[1] C.K.W. Tam, Computational acoustics: Issues and methods, AIAA Journal 33 (10) (1995) 1788–1796.
[2] F.Q. Hu, M.Y. Hussaini, J.L. Manthey, A low-dissipation and low dispersion Runge–Kutta scheme for computational acoustics, Journal of Computational Physics 124 (1996) 177–191.
[3] C.K.W. Tam, J.C. Webb, Dispersion-relation-preserving finite difference schemes for computational acoustics, Journal of Computational Physics 107 (1993) 262–281.
[4] S.K. Lele, Compact finite difference schemes with spectral-like resolution, Journal of Computational Physics 103 (1992) 16–42.
[5] L. Cueto-Felgueroso, I. Colominas, X. Nogueira, F. Navarrina, M. Casteleiro, Finite volume solvers and moving least-squares approximations for the compressible Navier–Stokes equations on unstructured grids, Computer Methods in Applied Mechanics and Engineering 196 (2007) 4712–4736.
[6] L. Cueto-Felgueroso, I. Colominas, High-order finite Volume methods and multiresolution reproducing kernels, Archives of Computational Methods in Engineering 15 (2) (2008) 185–228. doi:10.1007/s11831-008-9017-y.
[7] X. Nogueira, L. Cueto-Felgueroso, I. Colominas, H. Gómez, F. Navarrina, M. Casteleiro, On the accuracy of finite volume and discontinuous Galerkin discretizations for compressible flow on unstructured grids, International Journal for Numerical Methods in Engineering (2009) doi:10.1002/nme.2538.
[8] P. Lancaster, K. Salkauskas, Surfaces generated by moving least squares methods, Mathematics of Computation 87 (1981) 141–158.
[9] Wagner G.J., Liu W.K., Turbulence simulation and multiple scale subgrid models, Computational Mechanics 25 (2000) 117–136.
[10] N.B. Edgard, M.R. Visbal, A general buffer zone-type non-reflecting boundary condition for computational aeroacoustics, in: 9th AIAA/CEAS Aeroacoustics Conference and Exhibit, Hilton Head, AIAA, 2003, pp. 1–9 2003–3300.
[11] J.B. Freund, A proposed inflow/outflow boundary condition for direct computation of aerodynamic sound, AIAA Journal 35 (1997) 740–742.
[12] C. Bailly, D. Juvé, Numerical solution of acoustic propagation problems using Linearized Euler Equations, AIAA Journal 38 (1) (2000) 22–29.
[13] F.Q. Hu, On constructing stable perfectly matched layers as an absorbing boundary condition for Euler equations, AIAA paper 2003-3301, 2003.
[14] C. Bogey, C. Bailly, Acoustic Database, http://www.codiciel.fr/database/acoustic/acoustic.html.